

Supporting Information

Tuning the Oxidation State of SnO_x and Mass Transport to Enhance Catholyte-Free CO₂-to-Formate Electrolysis

*Taewoo Kim,^a Vivek S. Devalla,^a Sean P. Dunfield,^b Jack R. Palmer,^c Sara Dorr,^a Moses Kodur,^a Apoorva Gupta,^b and David P. Fenning^{*a,b,c}*

^aChemical Engineering Program, Department of Nanoengineering, University of California San Diego, La Jolla, California, 92093, United States

^bDepartment of Nanoengineering, University of California San Diego, La Jolla, California 92093, United States

^c Materials Science & Engineering Program, University of California San Diego, La Jolla, California 92093, United States

Corresponding Author

David P. Fenning

Email: dfenning@eng.ucsd.edu

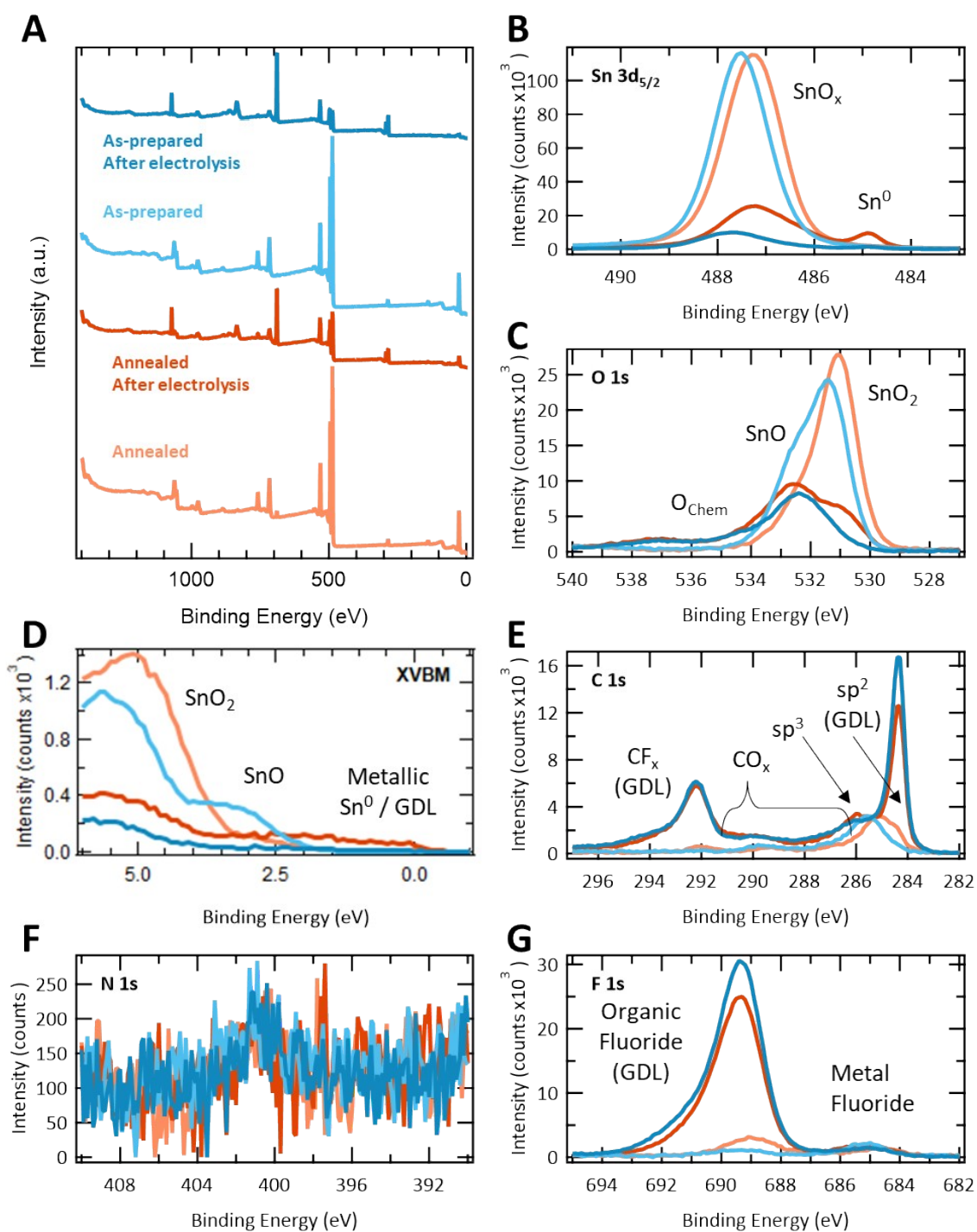


Figure S1. Electronic structure of the SnO_x electrodes. The light blue is as-prepared, the dark blue is as-prepared after 1 hr CO_2 electrolysis, the orange is the annealed, and the red is the annealed after 1 hr CO_2 electrolysis. (A) XPS survey spectra, (B) Sn 3d_{5/2}, (C) O 1s, (D) X-ray valence band maximum, (E) C 1s, (F) N 1s, and (G) F 1s XPS spectra of representative SnO_x films. All core levels have had a scalar background subtracted so that traces can be easily compared.

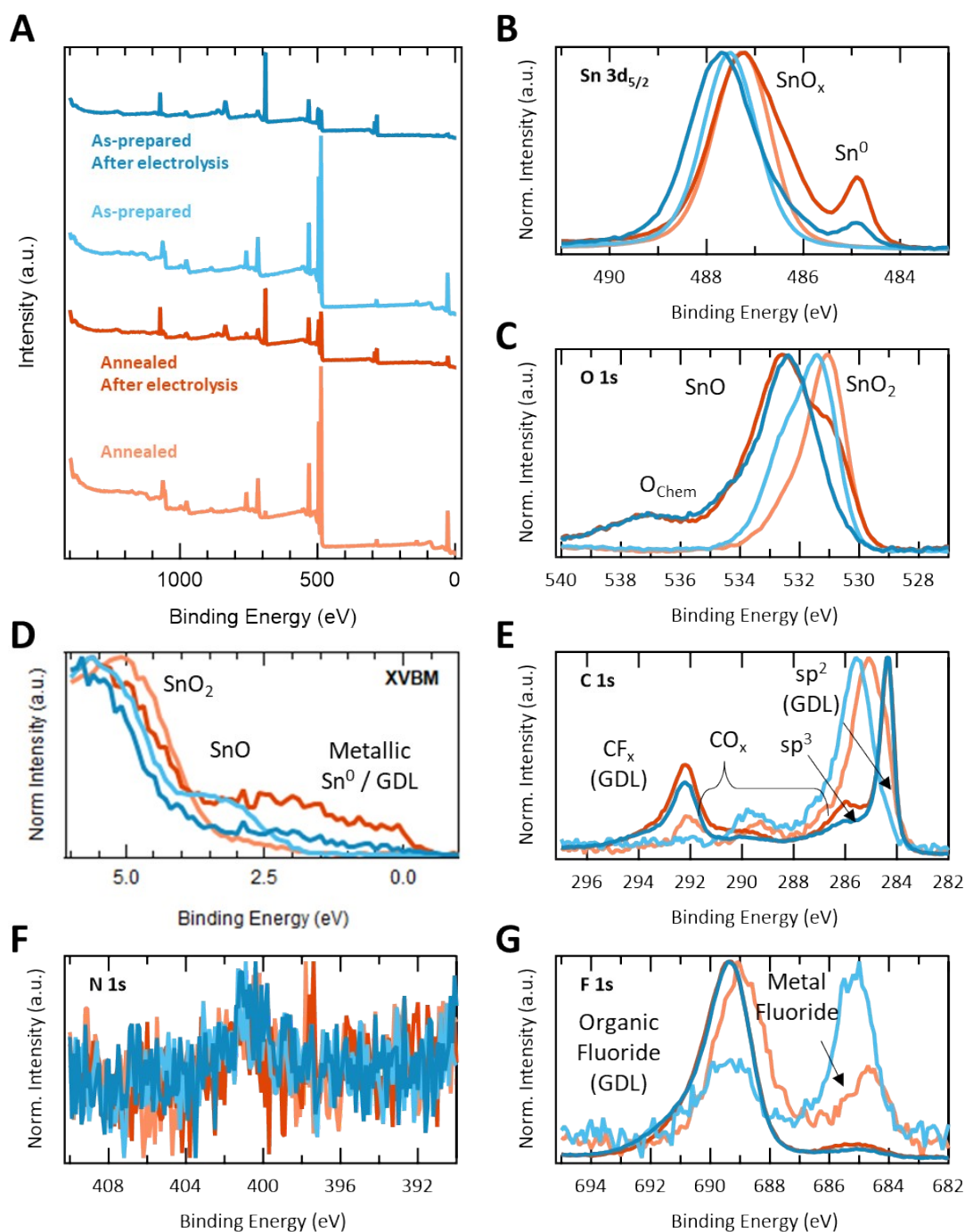


Figure S2. Electronic structure of the SnO_x electrodes (normalized). The light blue is as-prepared, the dark blue is as-prepared after 1 hr CO₂ electrolysis, the orange is the annealed, and the red is the annealed after 1 hr CO₂ electrolysis. (A) XPS survey spectra, (B) Sn 3d_{5/2}, (C) O 1s, (D) X-ray valence band maximum, (E) C 1s, (F) N 1s, and (G) F 1s XPS spectra of representative SnO_x films. All core levels have been normalized by baseline subtraction at the minimum value and scalar multiplication at the maximum so that the distribution of states within a given core level can be easily compared.

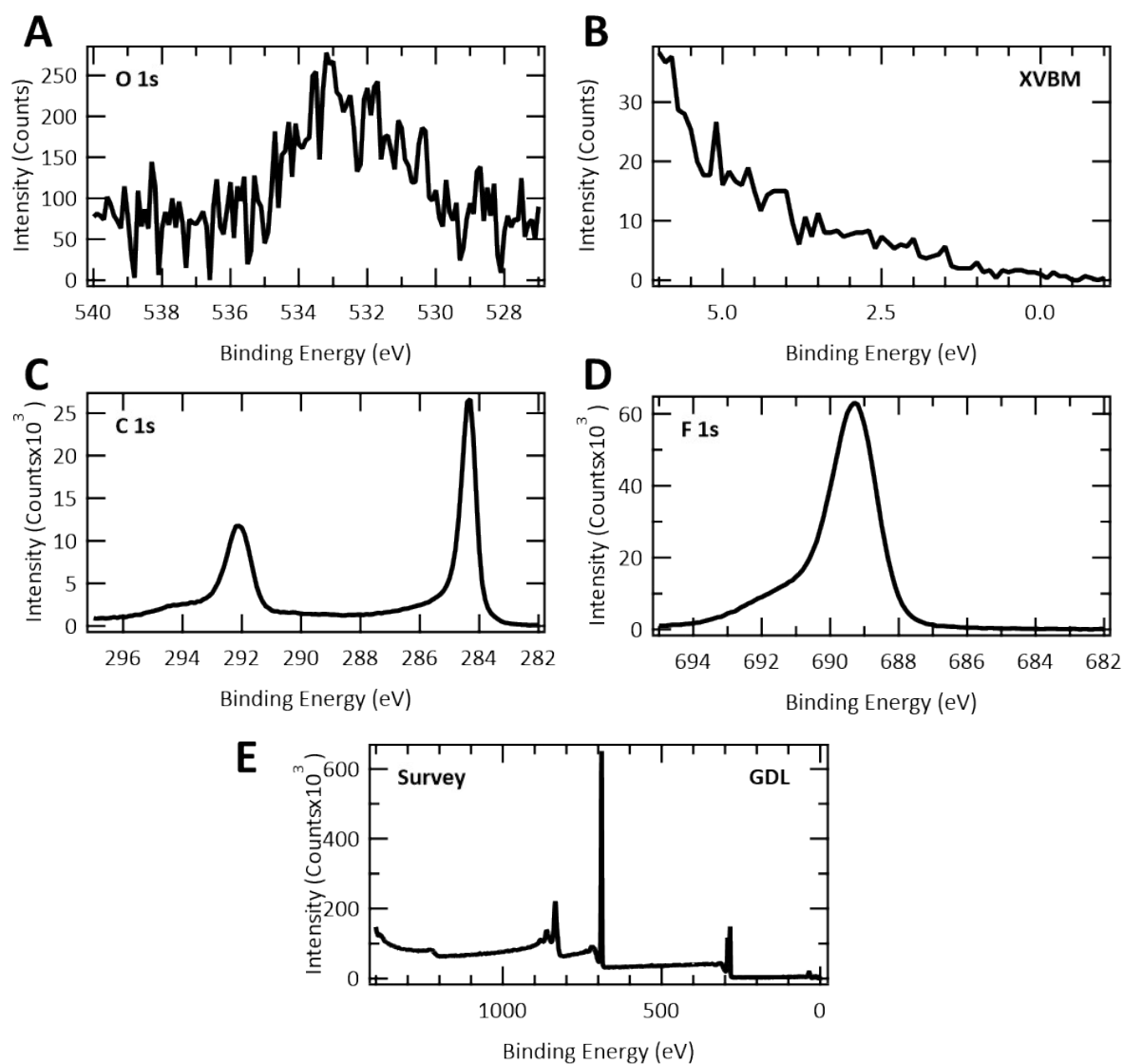


Figure S3. Electronic structure of the bare GDL. (A) O 1s, (B) X-ray valence band maximum, (C) C 1s, (D) F 1s, and (E) XPS survey spectra of bare GDL. All core levels have had a scalar background subtracted so that traces can be easily compared.

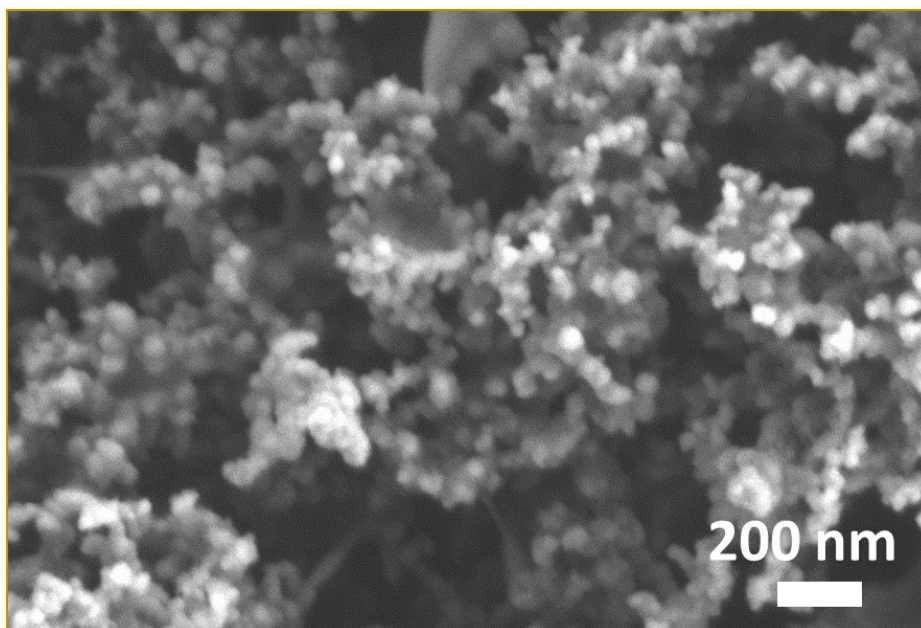


Figure S4. Scanning electron microscopy (SEM) image of bare gas diffusion layer (AvCarb GDS2230).

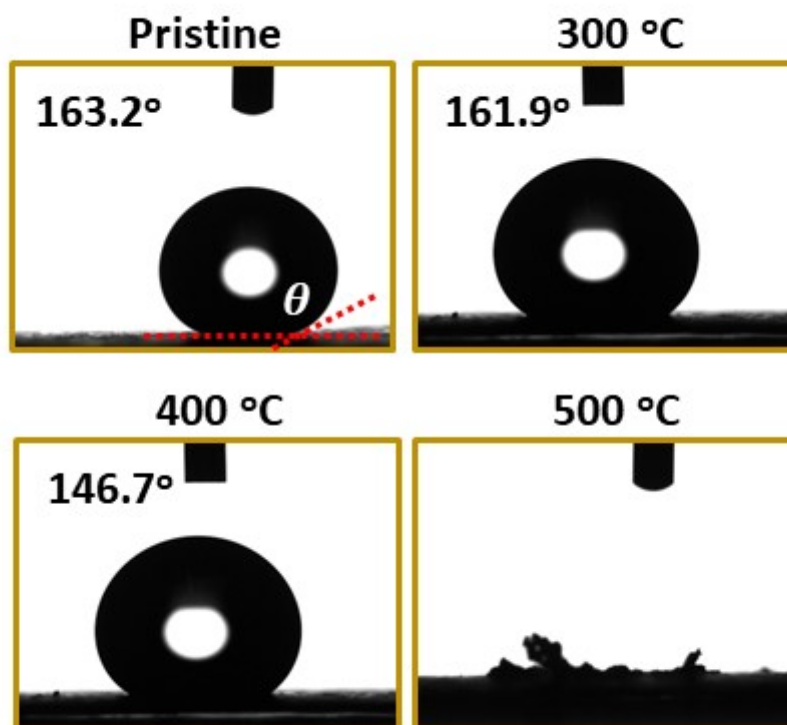


Figure S5. The contact angle of H₂O on the gas diffusion layers along with increasing annealing temperature. The contact angle on the GDLs annealed above 300 °C decreases or the surface is deformed during the measurement, indicating degradation of the structural property.

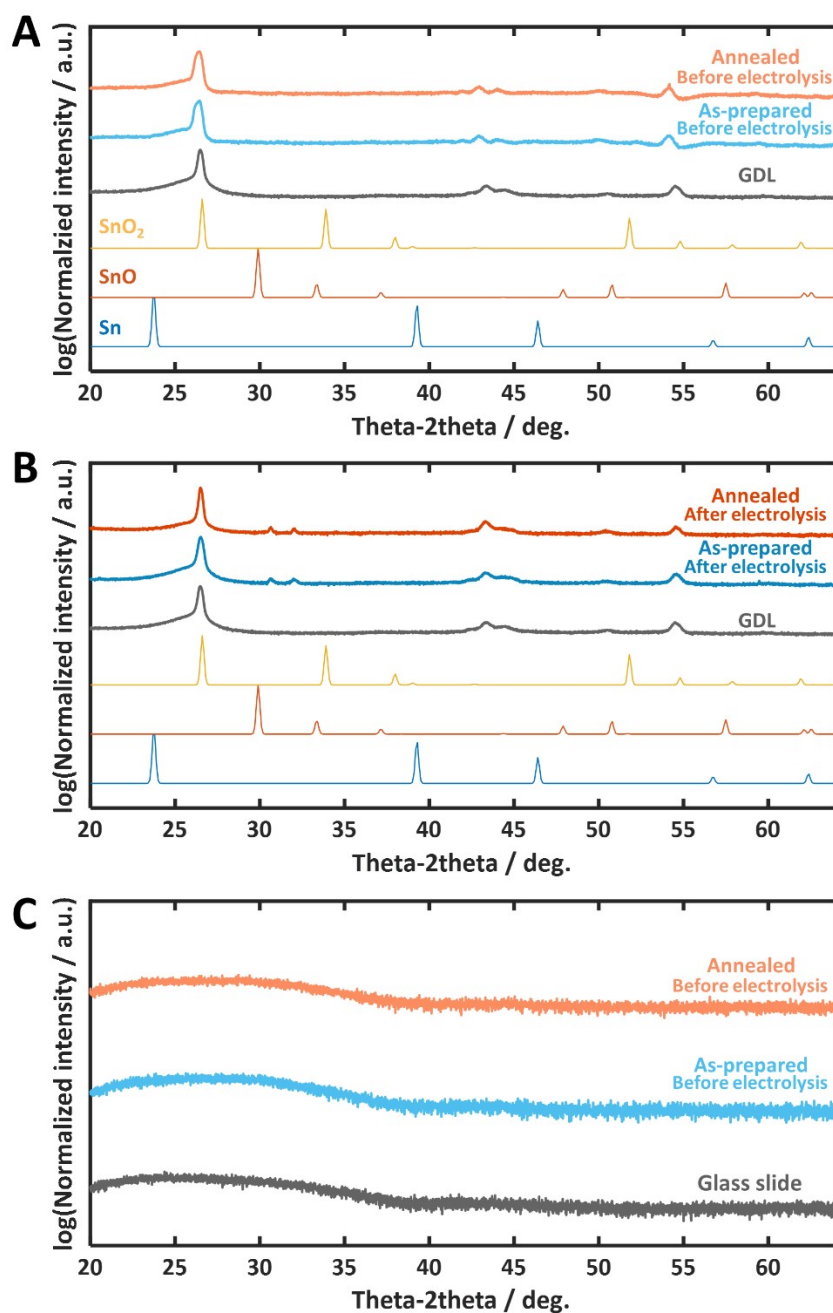


Figure S6. The crystalline structure of the SnO_x electrodes (A) before and (B) after electrolysis on gas diffusion layer and (C) the SnO_x electrodes on glass slides.

Diffractometry of bare gas diffusion layer and glass slide are included for comparison. Bragg diffraction angles are confirmed by using Sn (ICSD PDF No. 40-039), SnO (ICSD PDF No. 15-516), and SnO₂ (ICSD PDF No. 9-163) references. The diffraction at 30 and 31 deg. on both SnO_x catalysts after electrolysis in Figure S6B is appeared to be a minor bicarbonate crystal remaining on the surface of the SnO_x electrodes. The characteristic hump at lower deg. (< 40 deg.) on both SnO_x electrodes in Figure S6C indicates an amorphous nature of the SnO_x electrodes.

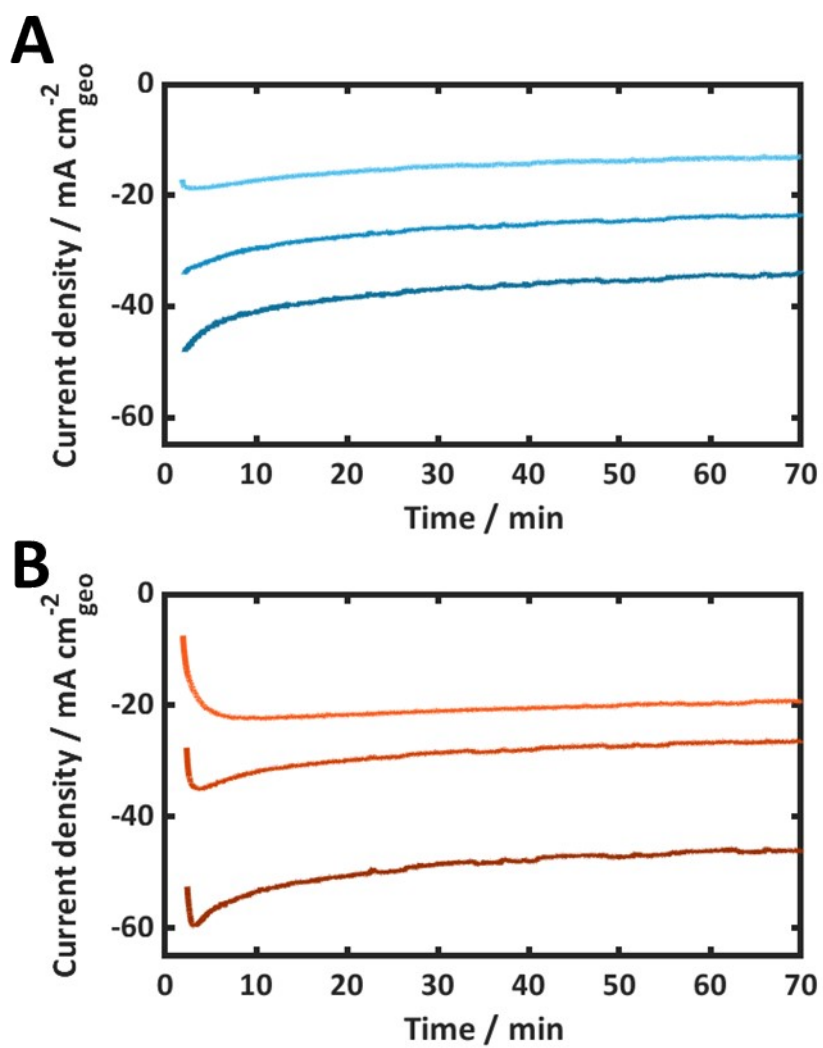


Figure S7. Current density profile with respect to electrolysis time. Catalyst with (A) an SnO-rich surface preparation and (B) an SnO₂-rich surface preparation. The cell voltages are 3.4, 3.2, and 3.0 V (from bottom to top per figure).

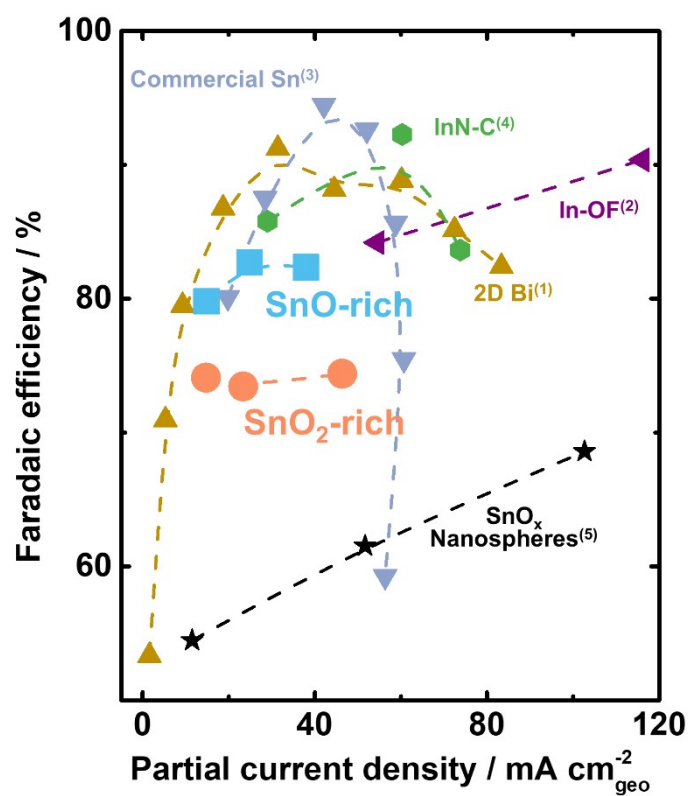


Figure S8. Comparison of Faradaic efficiency and geometric partial current density of formate on the SnO_x catalyst with the state-of-the-art catalysts (2D Bi¹, In-OF², commercial Sn³, InN-C⁴, and SnO_x nanospheres⁵).

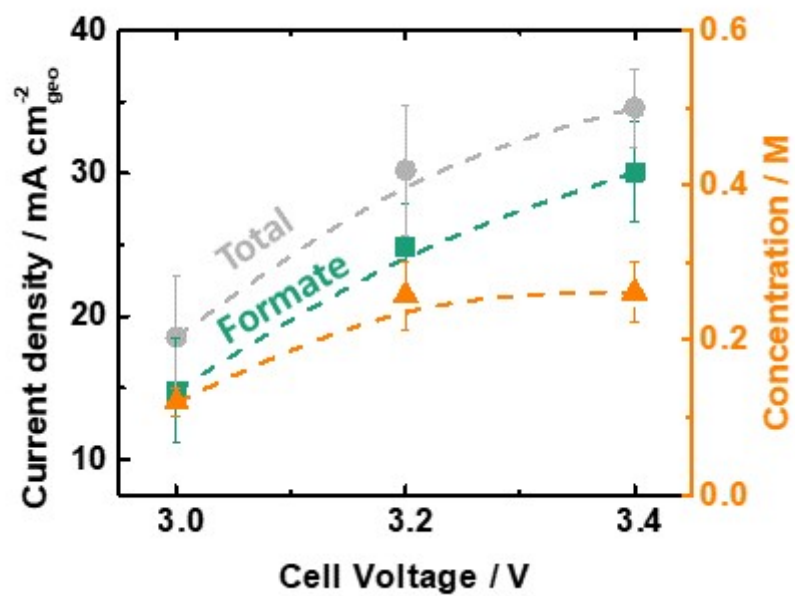


Figure S9. The current densities and concentration of formate as a function of cell voltage.

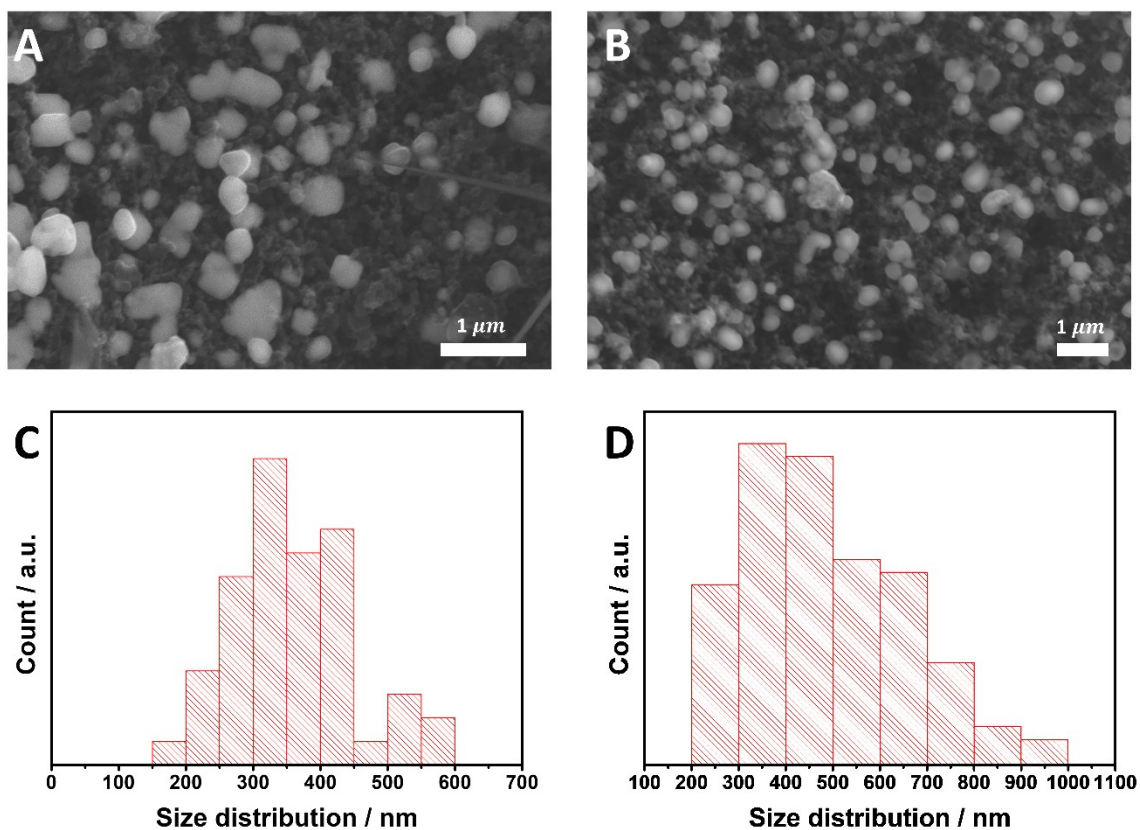


Figure S10. SEM images and size distribution of the catalyst prepared with an SnO-rich surface after extended period of electrolysis. (a) after 200 and (b) 300 min. Particle size distribution of (c) after 200 and (d) 300 min. The averaged particle sizes are 360 ± 89 and 488 ± 166 nm, respectively.

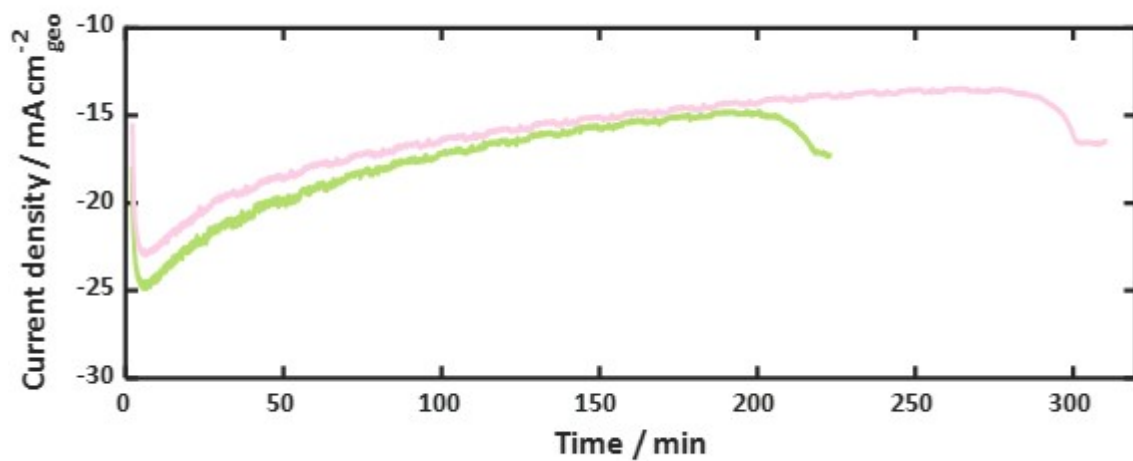


Figure S11. Current density profile of the extended period of electrolysis on the catalyst prepared with an SnO-rich surface at 3.0 V of cell voltage.

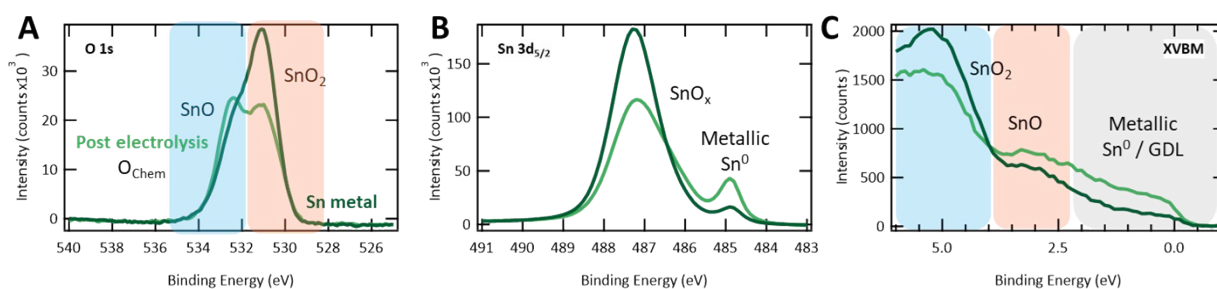


Figure S12. XPS of core level of (A) O 1s and (B) Sn 3d_{5/2}, and (C) X-ray valence band maximum (XVBM) spectra. An hour of CO₂ electrolysis is performed in 3 electrode system in a batch reactor, which consists of untreated Sn foil (working electrode), graphite rod (counter electrode), and Ag/AgCl/KCl(gel) (reference electrode) in CO₂-saturated 0.1 M KHCO₃ at 5 sccm of CO₂ flow rate.

We experimentally confirmed that SnO_x does not fully reduce to Sn⁰ during CO₂ electrolysis with a control experiment using a Sn metal foil with a native oxide (Figure S12). We performed CO₂ electrolysis on the untreated Sn metal foil (99.998% purity, Alfa Aesar) in a batch reactor to examine if a complete reduction of the native SnO_x was observed under CO₂ reduction environment. Before electrolysis, we confirmed that the surface of the untreated Sn metal foil consists of a native oxide with mixed SnO, SnO₂, and metallic Sn⁰ features via O 1s and Sn 3d_{5/2} core levels along with the XVBM spectra (dark green curves in Figure S12). After electrolysis, we found that the surface still mainly consists of SnO_x although some reduction of SnO_x is observed as evidence by: 1) an increase in the feature located within the higher binding energy region of the O 1s spectrum where SnO is expected (~533 eV), 2) an additional feature between the SnO_x and metallic Sn⁰ in Sn 3d_{5/2} (~486 eV) that is consistent with reduced SnO_x (e.g., SnO) and an increase in intensity of the Sn⁰ feature, and 3) a decreased ratio of SnO₂ (~530 eV) to SnO (~534 eV) and SnO_x (~487 eV) to metallic Sn⁰ (~485 eV) as compared to before electrolysis. Thus, the post-electrolysis XPS is sensitive to the characteristic electronic and chemical structure of both the SnO- and SnO₂-rich catalysts post-electrolysis rather than a regrown oxide and that the surface chemistry can therefore be interpreted with respect to the catalytic performance.

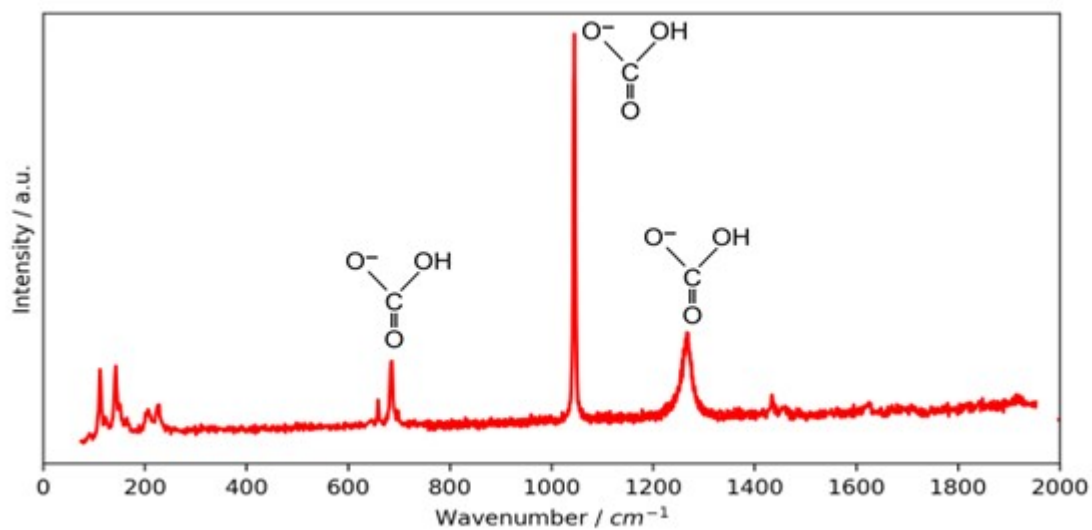


Figure S13. Post-electrolysis Raman Spectra. Raman spectra on the surface of a representative SnO_x catalyst after 1 hr of CO_2 electrolysis.

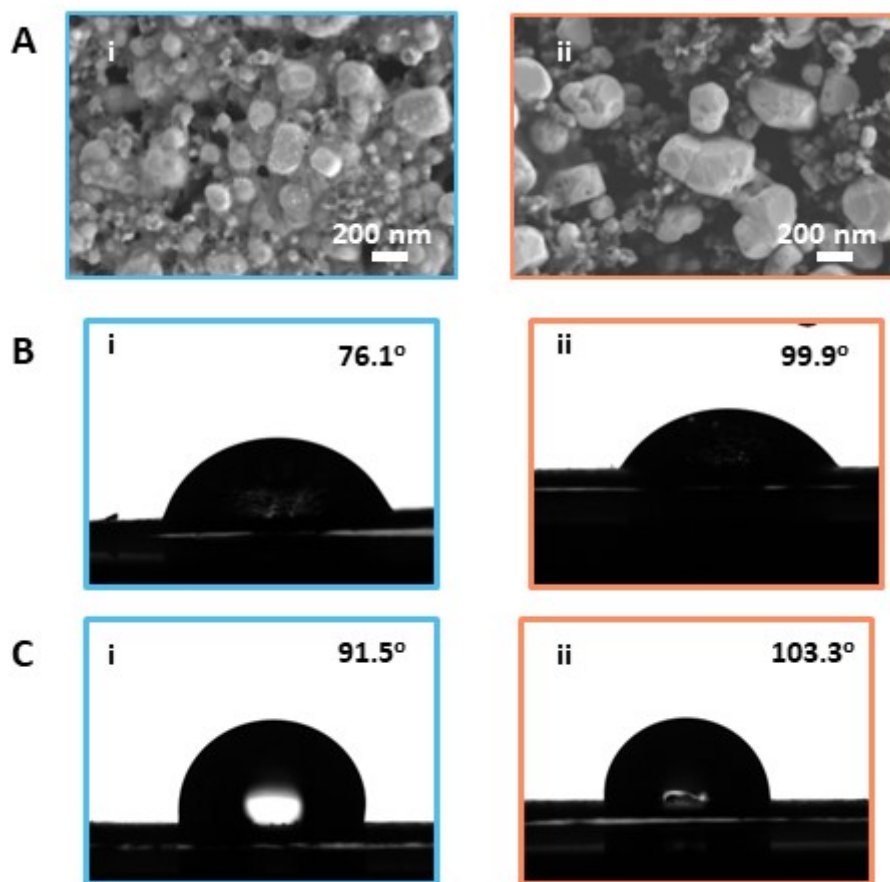


Figure S14. Post-electrolysis characterizations at 3.0 V of cell voltage for 1 hr. SEM images after electrolysis of catalysts prepared with A(i) SnO-rich surface A(ii) SnO₂-rich surface. The contact angle of H₂O on catalysts prepared with an SnO-rich surface B(i) before and C(i) after electrolysis and a SnO₂-rich surface B(ii) before and C(ii) after electrolysis.

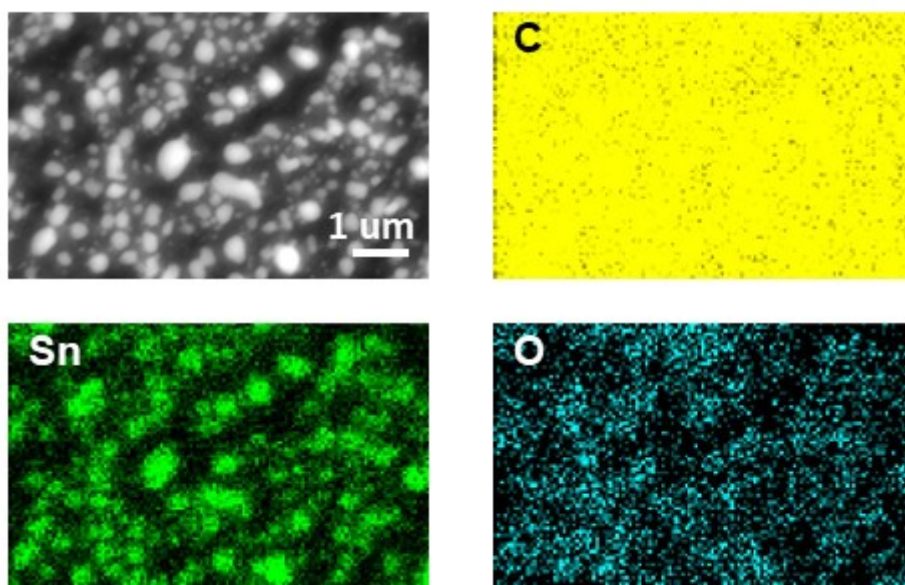


Figure S15. Post-electrolysis SEM-EDS on the catalyst prepared with an SnO-rich surface after electrolysis at 3.0 V of cell voltage for 1 hr.

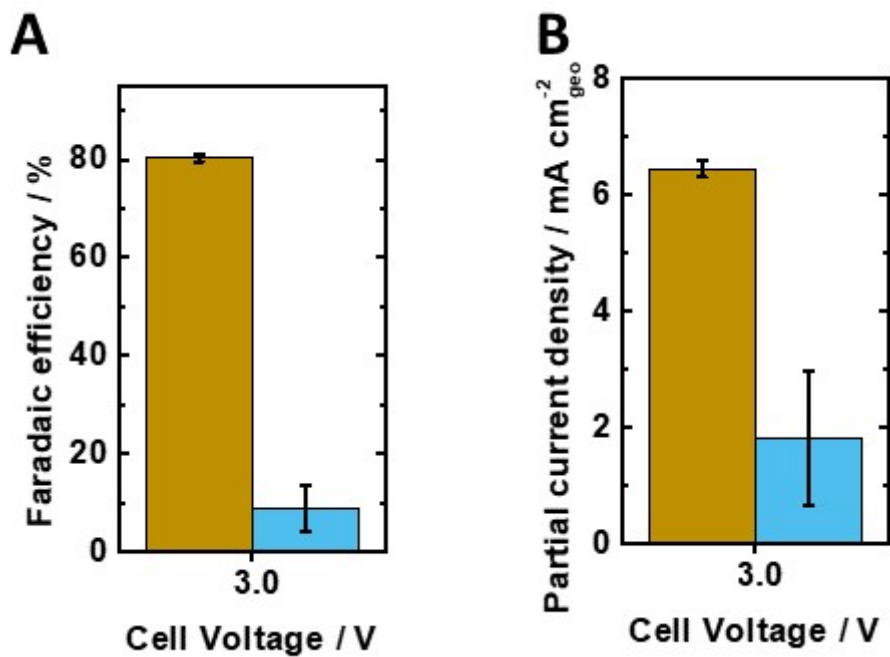


Figure S16. Comparison of hydrogen evolution on bare GDL (brown) and the catalysts prepared with an SnO-rich surface (light blue). No CO₂ reduction products are detected on the bare GDL. (A) Faradaic efficiency and (B) geometric partial current density of hydrogen.

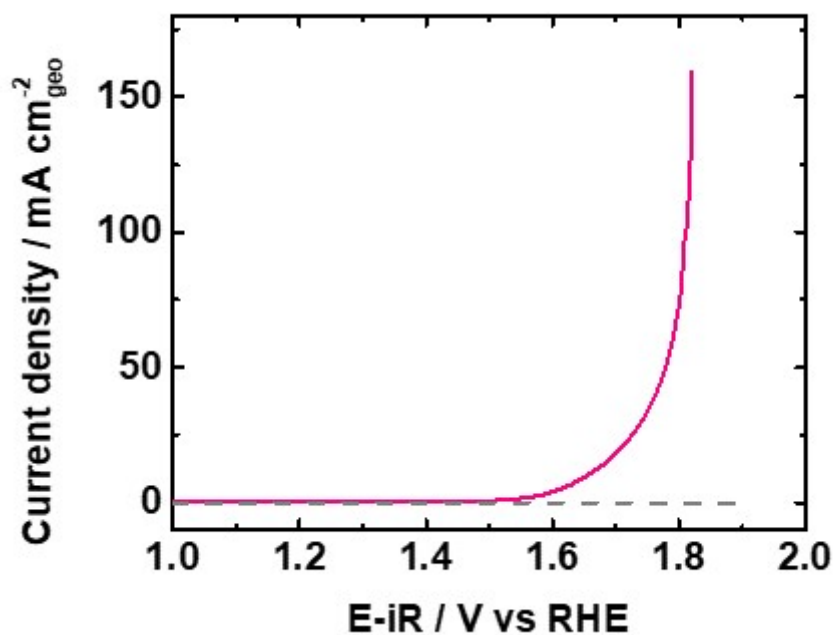


Figure S17. Anodic linear sweep voltammetry scans at 20 mV/s in 0.5 M sodium phosphate buffer solution (pH 3). The solid pink line is for IrO_x on Ti mesh electrode and the dashed gray line is for bare Ti mesh electrode. The estimated onset potential of oxygen evolution reaction on the IrO_x on Ti mesh electrode is 1.78 V vs RHE. Considering the thermodynamic overpotentials of CO₂-to-formate and oxygen evolution reaction (-0.12 and 1.23 V vs RHE, respectively), the estimated overpotential on the cathode at 3.0 V of cell voltage is 1.1 V.

Reference

- 1 C. Xia, P. Zhu, Q. Jiang, Y. Pan, W. Liang, E. Stavitski, H. N. Alshareef and H. Wang, *Nat. Energy*, 2019, **4**, 776–785.
- 2 Z. Wang, Y. Zhou, C. Xia, W. Guo, B. You and B. Y. Xia, *Angew. Chemie Int. Ed.*, 2021, **60**, 19107–19112.
- 3 W. Lee, Y. E. Kim, M. H. Youn, S. K. Jeong and K. T. Park, *Angew. Chemie*, 2018, **130**, 6999–7003.
- 4 P. Hou, X. Wang and P. Kang, *J. CO2 Util.*, 2021, **45**, 101449.
- 5 T. D. Nguyen-Phan, L. Hu, B. H. Howard, W. Xu, E. Stavitski, D. Leshchev, A. Rothenberger, K. C. Neyerlin and D. R. Kauffman, *Sci. Rep.*, 2022, **12**, 1–10.